LANGMUIR

Article

pubs.acs.org/Langmuir

Co–Cu Nanoparticles: Synthesis by Galvanic Replacement and Phase Rearrangement during Catalytic Activation

Raquel Nafria,[†] Aziz Genç,[‡,⊥] Maria Ibáñez,[†] Jordi Arbiol,[‡,§] Pilar Ramírez de la Piscina,[∥] Narcís Homs,*[,†,∥] and Andreu Cabot*[,†,§]

[†]Catalonia Institute for Energy Research, IREC, 08930 Sant Adrià del Besos, Spain

[‡]Catalan Institute of Nanoscience and Nanotechnology (ICN2), CSIC and The Barcelona Institute of Science and Technology (BIST), Campus UAB, Bellaterra, 08193 Barcelona, Catalonia, Spain

[§]Institució Catalana de Recerca i Estudis Avançats, ICREA, 08010 Barcelona, Spain

[∥]Departament de Química Inorgànica and Institut de Nanociència i Nanotecnologia, Universitat de Barcelona, 08028 Barcelona, Spain

[⊥]Metallurgy and Materials Engineering Department, Faculty of Engineering, Bartin University, 74100 Bartin, Turkey

Supporting Information

ABSTRACT: The control of the phase distribution in multicomponent nanomaterials is critical to optimize their catalytic performance. In this direction, while impressive advances have been achieved in the past decade in the synthesis of multicomponent nanoparticles and nanocomposites, element rearrangement during catalyst activation has been frequently overseen. Here, we present a facile galvanic replacement-based procedure to synthesize Co@Cu nanoparticles with narrow size and composition distributions. We further characterize their phase arrangement before and after catalytic activation. When oxidized at 350 °C in air to remove organics, Co@Cu core–shell nanostructures oxidize to polycrystalline CuO-Co_3O_4 nanoparticles with randomly distributed CuO and Co_3O_4 crystallites. During a posterior reduction treatment in H_2 atmosphere, Cu precipitates in a metallic core and Co migrates to the nanoparticle surface to form Cu@Co core–shell nanostructures. The catalytic behavior of such Cu@Co nanoparticles supported on mesoporous silica was further analyzed toward CO_2 hydrogenation in real working conditions.

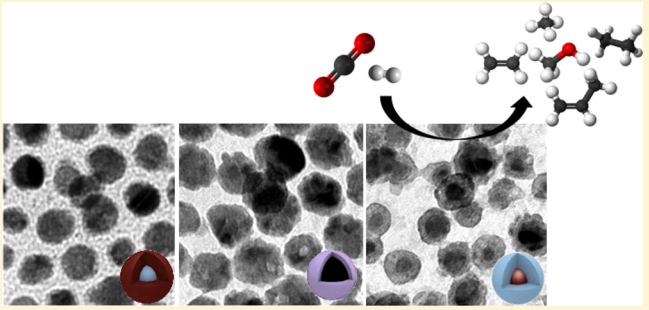

1. INTRODUCTION

The rational design of more active, selective, and durable catalysts requests for a deeper fundamental understanding of the influence of each material parameter on its performance. This ambitious goal requires engineering model catalysts with accurately tuned parameters and that can be tested in real working conditions. The availability of such real model systems is critical to overcome the material and pressure gaps partially disconnecting fundamental surface science studies from real industrial catalysts.[1−4] In this framework, colloidal synthesis routes allow producing large amounts of nanoparticles (NPs) with a unique control over composition, crystal phase, particle size, and surface facets.[5−9] Such colloidal NPs can be supported on or assembled into high surface area materials, and the resulting nanocomposites can be used as real catalytic model systems to investigate the influence of material parameters in real reaction conditions.[2,4,10−12] This strategy is especially interesting in multimetal catalysts, where not only the parameters of each individual component but also the distribution of these components, in the form of independent entities, multimetal alloys, Janus/dimer, or core–shell NPs, have a crucial role on the final catalytic performance.[1−4,13]

A particularly interesting catalytic reaction involving multicomponent heterogeneous catalyst and strongly influenced by the metal size and distribution is CO_2 hydrogenation:

$$CO_2 + xH_2 \rightarrow C_nH_{2n+1}OH + C_nH_{2n\pm2} + ...$$

The social and economic interest of CO_2 hydrogenation resides both on its potential to mitigate CO_2 concentration in the atmosphere and on the fact that CO_2 can be a feedstock of C_{2+} hydrocarbons and alcohols. Moreover, CO_2 is a nontoxic, noncorrosive, and nonflammable reactant, which can be easily stored and transported in liquid form under mild pressure.[14−18]

Among the numerous candidates for CO_2 hydrogenation, cobalt–copper catalysts are one of the most selective and cost-effective option.[19−26] Joint effects of Co and Cu can be understood on the basis of the properties of each single element

Received: December 29, 2015
Revised: February 14, 2016
Published: February 15, 2016

Downloaded via BARTIN UNIV on May 16, 2023 at 06:50:01 (UTC).
See https://pubs.acs.org/sharingguidelines for options on how to legitimately share published articles.

© 2016 American Chemical Society

DOI: 10.1021/acs.langmuir.5b04622
Langmuir 2016, 32, 2267−2276

catalyst. In the presence of H_2, Co is able to dissociate CO and CO_2 and to hydrogenate the resulting surface carbon species into hydrocarbons.[27,28] Thus, it is used for the synthesis of medium-chain and long-chain hydrocarbons in the Fischer−Tropsch (FT) process.[29] On the other hand, Cu molecularly adsorbs CO_2 and CO with a slow dissociation rate, which allows the incorporation of oxygen in the final hydrogenated products and thus the formation of alcohols.[27,28,30] Therefore, Cu is used in the synthesis of methanol from CO_2 hydrogenation or syngas.[31−34]

Previous studies on the use of Cu or Co catalysts for CO_2 hydrogenation and FT reactions demonstrated that parameters such as NP size strongly influence their performance. In particular, cobalt activity decreased rapidly when the NP size was reduced below 10 nm, although no size effect was observed on the selectivity.[35−39] On the other hand, the turnover frequencies for methanol formation from CO_2 hydrogenation of Cu NPs increased as NP size was reduced.[40] Beyond the properties of each individual catalytic material, the distribution of the active phases is also key to determine the composition of the FT and CO_2 hydrogenation product stream. As an example from the much better studied FT reaction, Subramanian et al. found that Co@Cu core−shell NPs were more active than Co−Cu dimer NPs in the CO hydrogenation, but Co−Cu NPs were more selective than Co@Cu NPs to the formation of ethanol and higher oxygenates.[27] Besides, Liu et al. reported that the hydrogenation of CO over Co@Cu NPs favored alcohol synthesis, while Cu@Co NPs generated more hydrocarbons.[24] Recently, Prieto et al. demonstrated that preventing the copper segregation on Co−Cu alloys increased the C_{2+} alcohols selectivity in the FT process.[41]

While catalytic performance is extremely sensitive to surface composition of the catalyst, an important challenge when dealing with multimetallic NPs is the characterization and understanding of the physical and chemical restructuring of the catalyst taking place during activation treatments and catalytic test. This is particularly crucial in Co−Cu NPs and in general in most transition metals, where activation/reduction processes inducing major chemical and structural changes are absolutely necessary, and major structural and chemical changes can take place during these processes as observed by Xiang et al.,[25] Carenco et al.,[42] and Alayoglu et al.[28] Nevertheless, due to the difficulties in producing catalysts with well-defined active phase distribution, shape, and size, the segregation and compositional reorganization of these catalytically active phases during catalyst activation are frequently overseen.

We present here a new synthetic strategy to produce monodisperse Co−Cu NPs with controlled metal ratios based on a galvanic replacement reaction. We used these NPs to gain understanding on the structural and chemical changes taking place before and after the thermal treatments used for the catalyst preparation and activation. We further analyze the catalytic behavior of these NPs supported on mesoporous silica toward CO_2 hydrogenation.

2. EXPERIMENTAL SECTION

Chemicals. Cobalt carbonyl ($Co_2(CO)_8$, ≥90%), copper(I) chloride (99.99%), copper(I) acetate (CuOAc, 97%), anhydrous 1,2-dichlorobenzene (DCB, 99%), and oleylamine (OLA, tech. 70%) were purchased from Sigma-Aldrich. Trioctylphosphine oxide (TOPO, 99%) was purchased from Strem Chemicals, trioctylamine (TOA, 97%) from Acros, and tetradecylphosphonic acid (TDPA, 97%) from PlasmaChem GmbH. All products were used without further purification, except for OLA which was distilled. Analytical grade isopropanol, ethanol, and hexane were purchased from Panreac. Stock solutions of copper(I) chloride in OLA (0.25 M) were prepared by dissolving 2.5 g of CuCl in 100 mL of OLA. All NP preparations were carried out using standard air-free techniques: a vacuum/dry-argon Schlenk line was used for the synthesis and an argon-filled glovebox for storing and handling air- and moisture-sensitive chemicals.

Cobalt Nanoparticles. Co NPs were produced following a similar procedure as the one described previously by Puntes et al.[43] but replacing oleic acid by OLA. In a typical synthesis, 0.1 g of TOPO, 15 mL of DCB, and 0.3 mL of OLA were degassed in a 250 mL three-neck flask for 30 min in Ar. Then the solution was heated to 180 °C. At this temperature, 0.54 g of $Co_2(CO)_8$ dissolved in 3 mL of DCB was rapidly injected. After 10 min, the solution was cooled down to room temperature. Co NPs were purified by multiple precipitation/redispersion steps using isopropanol as a nonsolvent and hexane as solvent.

Copper Nanoparticles. Cu NPs were prepared following the procedure reported by Yang et al.[44] In a typical synthesis, 10 mL of TOA was added in a 50 mL three-neck flask and heated to 130 °C for 30 min under Ar atmosphere. After cooling to room temperature, 0.246 g of CuOAc and 0.556 g of TDPA were placed into the flask. The mixture was heated up to 180 °C and maintained at this temperature for 30 min. Afterward, the reaction temperature was further increased to 270 °C and kept for another 30 min, before cooling down to ambient temperature. Cu NPs were purified by multiple precipitation/redispersion steps using methanol as a nonsolvent and hexane as solvent.

Cobalt−Copper Nanoparticles. Co−Cu NPs were produced by a one-pot, two-step procedure. First, Co NPs were synthesized following the above procedure. In a second step, inside the 250 mL three-neck flask containing the Co NPs, different volumes of stock solution of Cu^+ ions in OLA (0.25 M) were added at room temperature (6.25 mL to produce $Co_{0.6}$−$Cu_{0.4}$ NPs and 12.5 mL to get $Co_{0.3}$−$Cu_{0.7}$ NPs). Then the mixture was heated up to 180 °C and maintained at this temperature for 30 min. Afterward, the solution was cooled down, and NPs were purified by three hexane/isopropanol redispersion/precipitation cycles. NPs nomenclature (Co_x−Cu_y) indicates the Co/Cu molar relation ([Co/Cu] = x/y).

SiO_2-Supported Nanoparticles. Metal NPs were incorporated via capillary inclusion to a mesoporous hydrophobic SiO_2 support with a surface area of 191 m^2/g and an average pore size of 21 nm (AEROSIL R-9200 hydrophobic silica).[28,45] In a typical preparation, 2 g of SiO_2 was added to a hexane solution containing 200 mg of NPs (∼150 mg of NPs after ligand removal). The slurry was sonicated for 2 h at room temperature to facilitate the introduction of NPs within the silica pores. After that, hexane was evaporated under vacuum. Before catalyst characterization and catalytic test, the nanopowder was annealed at 350 °C for 4 h in air flow to remove organics.

Materials Characterization. X-ray diffraction (XRD) patterns were obtained on a Bruker D8 automated diffractometer, equipped with a primary monochromator and a LynxEye detector and using Cu Kα radiation (λ = 1.5406 Å). The instrument resolution was 0.05° in 2θ, the studied range was between 35° and −55°, and the acquisition time for each sample was set to 2 h 20 min. Metal contents were determined using optical emission spectroscopy by means of inductively coupled plasma (ICP) on a PerkinElmer Optima 3200 RL system. The specific surface area of the materials was determined by N_2 adsorption at 77 K using a Tristar II 3020 Micromeritics system. Thermogravimetric analyses (TGA) were performed in the temperature range of 30−700 °C at a heating rate of 5 °C min^{-1} under air using a PerkinElmer TGA4000. Transmission electron microscopy (TEM) and high-resolution TEM (HRTEM) micrographs were obtained using a Carl ZEISS LIBRA 120 microscope operated at 120 keV and a field emission gun (FEG) FEI Tecnai F20 microscope operated at 200 keV, respectively. Scanning TEM (STEM)−electron energy-loss spectroscopy (EELS) and STEM−energy dispersive X-ray spectroscopy (EDX) analyses are conducted on the Tecnai microscope equipped with high angle annular dark field (HAADF) and EDX detectors and a Quantum Gatan image filter (GIF). EDX analyses were performed with an EDAX Octane T Ultra W/Apollo

DOI: 10.1021/acs.langmuir.5b04622
Langmuir 2016, 32, 2267−2276

XLT2 SDD. The software used to interpret the images was the FEI TEM Imaging & Analysis (TIA).

Hydrogen temperature-programmed reduction (TPR) was performed using a Micromeritics AutoChem HP 2950 chemisorption analyzer. 50 mg of sample was pretreated at 90 °C for 30 min under flowing He (50 mL/min). After cooling to room temperature, the samples were reduced in a flow of 12 vol % H_2/Ar (50 mL/min), and temperature was linearly increased at a rate of 10 °C/min up to 800 °C.

The Cu^0 surface area was determined by dissociative N_2O adsorption using a Micromeritics AutoChem HP 2950 chemisorption analyzer. 50 mg of each sample was pretreated at 90 °C for 30 min under flowing He (50 mL/min). After cooling to room temperature, samples were reduced in a flow of 12 vol % H_2/Ar (50 mL/min), and temperature was linearly increased at a rate of 10 °C/min up to 350 °C at 30 bar. Again after cooling at 35 °C, samples were oxidized in a flow of 6% N_2O/He (10 mL/min) for 1 h. Finally, samples were flushed with He to remove the oxidant and cooled to room temperature to start another TPR run. The exposed Cu surface area (S_{Cu}) in the reduced catalysts was calculated on the basis of $Cu/N_2O = 2$ titration stoichiometry and a surface atomic density of 1.4×10^{19} Cu atoms per m^2.

Catalytic Behavior. Catalytic tests were carried out in a Micro-activity-Reference unit (PID Eng&TECH) in the temperature range 280−350 °C at 30 bar. 100 mg of catalyst was mixed with inactive SiC (Prolabo, 0.5 mm) and placed in a tubular fixed-bed reactor (305 mm long, 9 mm i.d., 316 L stainless steel) up to a catalytic bed volume of 1 mL. The temperature was measured by a thermocouple in direct contact with the catalytic bed. Before the reaction, the catalyst was *in situ* reduced using a mixture of 12% vol/vol H_2/Ar; temperature and pressure were linearly increased at 350 °C and 30 bar for 1 h and then kept at these conditions for another 30 min. Thereafter, the pressure was kept at 30 bar and the temperature was decreased to 280 °C. Then the catalyst was exposed to a reactant gas mixture of $CO_2/H_2 = 1/3$ balanced with 20% of N_2, as an internal standard, under a gas hourly space velocity (GHSV) of 3000 h^{-1}. After a period of 4 h at 280 °C, the reaction temperature was consecutively increased to 300, 320, 340, and 350 °C and maintained at each temperature for 4 h. After each temperature change, the system was stabilized for 1 h, and then the corresponding initial activity at a given temperature was determined. The products were analyzed online with a GC system (Varian 450-GC) equipped with a methanizer, TCD, and FID detectors. CO_2 conversion (X_{CO_2}) and the selectivity (S_i) for each product (excluding H_2O) were calculated according to

$$X_{CO_2} = \frac{\sum n_i P_i}{[CO_2] + \sum n_i P_i}$$

$$S_i = \frac{n_i P_i}{\sum n_i P_i}$$

where P_i and n_i are the molar concentration and the number of carbon atoms of a specific product in the outlet gas, and $[CO_2]$ is the CO_2 molar concentration in the outlet gas. The relative selectivities of the catalysts toward the formation of hydrogenated products were calculated as S_i, but excluding CO.

3. RESULTS AND DISCUSSION

Co−Cu NPs were produced by a one-pot, two-step procedure. First, Co NPs were obtained by $Co(CO)_8$ decomposition in the presence of TOPO and OLA at 180 °C. After 10 min reaction, the solution was cooled down to room temperature, and spherical Co NPs with an average size of 10 nm were obtained (Figure 1a). Then, Cu^+ ions were added to the Co NPs solution, and the mixture was heated up again to 180 °C. After 30 min reaction, slightly larger spherical NPs were obtained (Figure 1c). HRTEM micrographs showed the presence of Moiré fringes in the final Co−Cu NPs, pointing toward the superposition of two crystalline structures (Figure 1d). In the shell, the (011) and (111) planes of cuprite Cu_2O with 2.44 and 2.98 Å distances

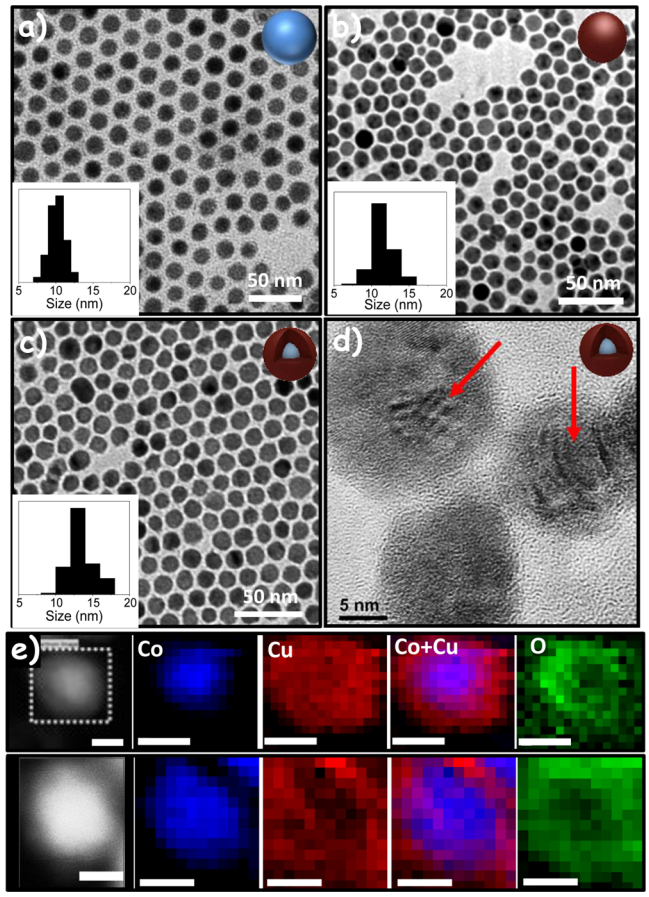

Figure 1. (a−c) TEM micrographs and size histograms (insets) of the Co (a), Cu (b), and $Co_{0.6}@Cu_{0.4}$ (c) NPs. (d) HRTEM micrograph of Co@Cu NPs. (e) Two examples of HAADF (Z-contrast) images and Co, Cu, and O EELS compositional maps of $Co_{0.6}@Cu_{0.4}$ NPs. Scale bars correspond to 5 nm.

could be evidenced. EELS elemental maps revealed the final Co−Cu NPs to be composed by a Co core and a partially oxidized Cu shell (Figure 1e), although a minor alloying cannot be discarded. The shell oxidation was associated with the NPs interaction with air during purification and during the preparation and transportation of TEM grids.

The Co core clearly shrank with the Cu^+ introduction, up to the point that when an excess amount of Cu^+ ions was introduced, Co was totally dissolved and pure Cu NPs were obtained. On the other hand, the injection of the Cu precursor in the exact same reaction conditions but in the absence of Co NPs did not result in the formation of Cu NPs. These experimental facts evidenced that the Cu shell grew by the galvanic replacement of Co by Cu^+ ions in solution.[46] This replacement was driven by the larger reduction potential of Cu^+ compared with Co^{2+} (at 25 °C and 1 atm, $E°(Co^{2+}/Co) = -0.28$ V; $E°(Cu^+/Cu) = 0.52$ V). While galvanic replacement generally results in the formation of porous structures, the relatively high reaction temperatures used here (180 °C) could allow the formed vacancies to diffuse to the surface, thus finally resulting in solid NPs. Because oxidation of each Co atom required the reduction and incorporation of two Cu^+ ions, increasingly larger NPs were obtained when increasing the Cu-to-Co ratio. Such a synthetic strategy allowed to carefully adjust the metal composition of the final NPs and to produce Co−Cu NPs

DOI: 10.1021/acs.langmuir.5b04622
Langmuir 2016, 32, 2267−2276

with the full range of Cu content by introducing the required precise amounts of copper ions..

Owing to the core−shell nature of the Co−Cu NPs produced by the galvanic replacement strategy, we refer to them using the nomenclature: $Co_x@Cu_{1-x}$, where x and $1 - x$ respectively denote the Co and Cu atomic ratio within the NP. We will maintain this nomenclature even after thermal treatment of the NPs in oxidizing or reducing atmospheres, which, as detailed below, clearly change the NP composition and phase distribution.

As a reference for the chemical, structural, and functional characterization of the Co@Cu NPs, 10 nm Co NPs were also prepared by the same procedure (first step), and 10 nm spherical Cu NPs were prepared following Yang et al.'s procedure (Figure 1b).[44]

Figure 2 shows the XRD patterns of Co, Cu, and two Co@Cu samples with different Co/Cu molar ratio: $Co_{0.6}@Cu_{0.4}$ and

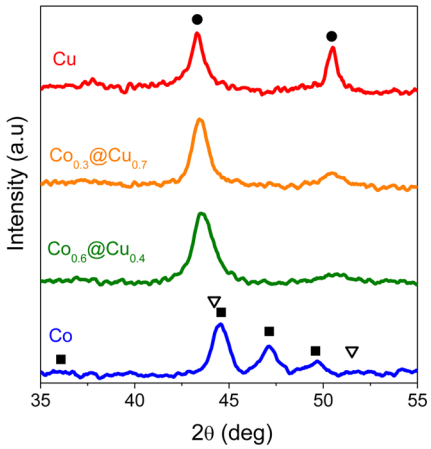

Figure 2. XRD patterns of Co, $Co_{0.6}@Cu_{0.4}$, $Co_{0.3}@Cu_{0.7}$, and Cu unsupported nanoparticles. Peaks corresponding to (■) ε-Co,[47] (▽) Co fcc (JCPDS 15-0806), and (●) Cu fcc (JCPDS 89-2838) are marked as a reference.

$Co_{0.3}@Cu_{0.7}$. Co and Cu NPs crystallized in the ε-Co and face-centered cubic (fcc, JCPDS 89-2838) phases, respectively.[47] However, Co@Cu NPs did not display the ε-Co phase but showed a XRD pattern that resembled a fcc phase with lattice parameters in between those of Co and Cu fcc phases. We speculate that the metastable ε-Co phase transformed to the stable Co_{fcc} during the additional 30 min treatment at 180 °C used to grow the Cu shell. A slight Co−Cu alloying could help in this direction, although the solubility of the two metals is very low in the temperature range here considered.[28,42,48−50]

Five model catalysts were prepared by capillary inclusion of colloidal NPs (7 wt %) into mesoporous hydrophobic SiO_2: (i) Co/SiO_2, (ii) Cu/SiO_2, (iii) Co/SiO_2 + Cu/SiO_2 physical mixture (50 wt %), (iv) $Co_{0.6}@Cu_{0.4}/SiO_2$, and (v) $Co_{0.3}@Cu_{0.7}/SiO_2$. Organic capping agents from the NP surface were thermally decomposed in air for 4 h at 350 °C. This temperature was selected on the basis of TGA (Supporting Information Figure SI1). The composition of the final catalysts, calculated by ICP, is displayed in Table SI1.

Figure 3a shows a low-magnification HAADF STEM micrograph of the $Co_{0.3}@Cu_{0.7}/SiO_2$ sample after thermal treatment in air. High contrast $Co_{0.3}@Cu_{0.7}$ NPs can be identified within the lower contrast SiO_2 matrix. While most NPs were found individually distributed over the SiO_2 surface, some aggregation was also observed. Because of this slight aggregation, we discarded the Co + Cu/SiO_2 catalyst, with a mixture of Co and Cu NPs simultaneously incorporated in the same support, as a reference material, as it contained an uncontrolled combination of independent Cu and Co NPs and aggregates of Co + Cu NPs.

HRTEM analysis (Figure 3b, Figures SI2 and SI3) showed the oxidized core−shell NPs to be polycrystalline. Power spectrum analysis revealed the presence of the fcc Co_3O_4 and/or a $Co_{3-x}Cu_xO_4$ phase across the NP. Spinel cubic phase has a general formula AB_2O_4, where A and B correspond to tetrahedral and octahedral cation sites, respectively, in a cubic close packing of oxygen. Cu^{2+} may substitute cobalt cations and result in the $Co_{3-x}Cu_xO_4$ spinel phase. While Co_3O_4 and $Co_{3-x}Cu_xO_4$ phases could not be differentiated due to their small lattice parameter differences, the random distribution of phases and metals within each NP already pointed toward the interdiffusion of the two elements, Co and Cu, during oxidation at 350 °C.

The nature of the oxide phases formed after oxidation was further analyzed by XRD (Figure 4). In the monometallic catalysts, Co/SiO_2 and Cu/SiO_2, main diffraction peaks of Co_3O_4 spinel phase (JCPDS 42-1467) and CuO monoclinic phase (JCPDS 05-0661) were identified, respectively. The Co/SiO_2 + Cu/SiO_2 catalyst showed the peaks corresponding to the same oxide phases detected in monometallic samples. In the $Co@Cu/SiO_2$ catalysts, XRD peaks corresponding to the CuO monoclinic phase were clearly identified. Furthermore, diffrac-

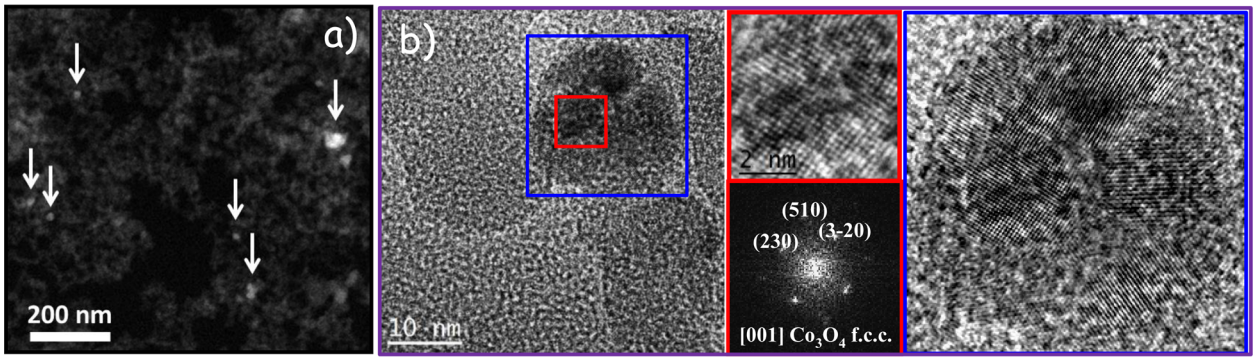

Figure 3. (a) Low-magnification HAADF-STEM micrograph of $Co_{0.3}@Cu_{0.7}/SiO_2$. Arrows point at the higher contrast Co@Cu NPs. (b) HRTEM micrograph showing a polycrystalline oxidized $Co_{0.3}@Cu_{0.7}$ NP. A detail of the blue region clearly shows the NP polycrystallinity. A detail of the red squared region and its corresponding power spectrum shows a Co_3O_4 or $Co_{3-x}Cu_xO_4$ fcc phase (space group = *Fd*3-*ms*) with lattice parameter a = 0.814 nm and visualized along its [001] zone axis.

DOI: 10.1021/acs.langmuir.5b04622
Langmuir 2016, 32, 2267−2276

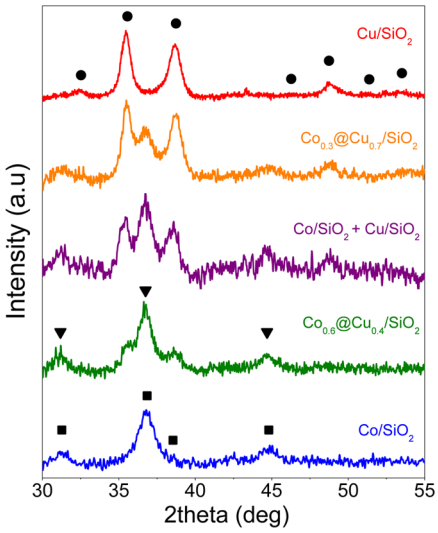

Figure 4. XRD patterns of the Co/SiO_2, Cu/SiO_2, $Co/SiO_2 + Cu/SiO_2$, $Co_{0.6}@Cu_{0.4}/SiO_2$, and $Co_{0.3}@Cu_{0.7}/SiO_2$ catalysts after oxidation at 350 °C. The peaks corresponding to (■) Co_3O_4 (JCPDS 42-1467), (▼) Co_2CuO_4 (JCPDS 37-0878), and (●) CuO (JCPDS 05-0661) are marked as a reference.

tion peaks at 31.2°, 36.7°, and 44.7° could be assigned to the presence of Co_3O_4 and/or $Co_{3-x}Cu_xO_4$ in spinel phase. From the ratio between the CuO and the Co_3O_4 XRD peaks obtained from the 50% $Co/SiO_2 + Cu/SiO_2$ sample and considering 50% of each CuO and Co_3O_4 in this material, we estimated the $Co_{3-x}Cu_xO_4$ spinel phase could account for up to a 10% of the Cu atoms in the $Co_{0.3}@Cu_{0.7}/SiO_2$ and up to a 20% of the Cu in the $Co_{0.6}@Cu_{0.4}/SiO_2$.

Figure 5 shows the TPR profiles measured from the different catalysts. The Co/SiO_2 catalyst was characterized by a two-step

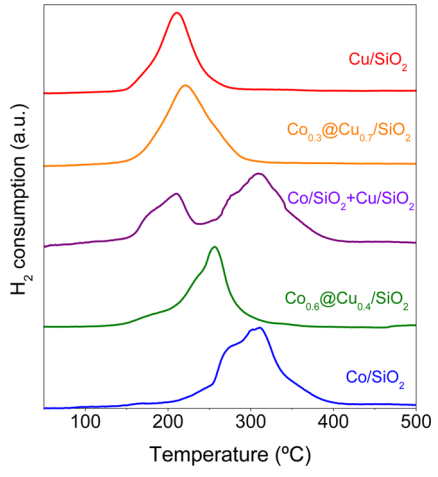

Figure 5. H_2 temperature-programmed reduction profiles of Co/SiO_2, Cu/SiO_2, $Co/SiO_2 + Cu/SiO_2$, $Co_{0.6}@Cu_{0.4}/SiO_2$, and $Co_{0.3}@Cu_{0.7}/SiO_2$ catalysts.

reduction profile with maxima of hydrogen consumption at 275 and 311 °C: $Co_3O_4 \rightarrow CoO \rightarrow Co$.[51−53] The reduction profile of Cu/SiO_2 was essentially characterized by a broad peak at lower temperatures than CoO, with a maximum of hydrogen consumption at 210 °C.[53,54] The TPR profile of the $Co/SiO_2 + Cu/SiO_2$ sample showed the peaks associated with the independent reduction of pure oxides, Co_3O_4 and CuO, which suggested no interaction or promotional effect between the two elements. On the other hand, $Co@Cu/SiO_2$ catalysts were characterized by a unique reduction peak at temperatures in between those of Co/SiO_2 and Cu/SiO_2 catalysts, which shifted toward lower temperatures when increasing the Cu content in the NP. This confirmed a synergistic effect in the reduction of both species, where Cu probably promoted the Co^{n+} reduction, and suggested an intimate contact of the cobalt and copper species and a good sample homogeneity.[53−56]

To further study the structural and chemical evolution of the Co@Cu NPs during oxidation and reduction treatments, TEM analysis of the NPs supported on a silicon nitride grid was carried out after each thermal treatment. Figure 6 shows TEM micrographs of the exact same $Co_{0.3}@Cu_{0.7}$ NPs just after their preparation (Figure 6a), after oxidation at 350 °C for 4 h in air (Figure 6b), and after reduction at 350 °C and 30 bar in a 12% H_2−Ar (Figure 6c). After the thermal treatment in air, slightly larger polycrystalline NPs with no clear contrast between a hypothetical core and a shell were identified. Some voids were observed within the NPs after oxidation, which we assigned to the nanoscale Kirkendall effect and pointed toward a faster diffusion of Co and/or Cu than oxygen through the growing metal oxide shell (Figure SI4).[57−60]

After the reduction treatment, NPs shrank and a core−shell structure was recovered. HRTEM and EDS analysis showed the reduced NPs to be formed by a polycrystalline CoO shell and a metallic Cu core (Figure 7, Figures SI5−SI7). Taking into account the hydrogen consumed from TPR results, we believe that the cobalt oxide shell was completely reduced during the H_2 treatment, but it oxidized when exposed to air before TEM analysis.

According to this experimental evidence, we hypothesize that during the oxidation treatment the diffusion of cobalt through an initially formed CuO shell takes place, leaving a void within the particle. With the reduction treatment, metal copper collapsed to the center of the NP and Co remained at its surface. Upon exposure to air during TEM sample preparation and transportation, Co was oxidized into a thicker and lower contrast CoO shell than that of the initial Co@Cu NPs. This explains the different electron microscopy contrast between the as-produced Co@Cu NPs and the reduced ones. Notice finally that in spite of the diffusion of the different components within each individual particle, resulting in an inversion of the core−shell structure, NPs supported on SiN_x did not coalesce or aggregate. These results are slightly different from those obtained by Somorjai and collaborators, who studied the compositional reorganization of Cu@Co NPs, observing the surface segregation of Cu during oxidation, the surface segregation of Co during reduction, and the formation Cu−Co dimers after the redox conditioning.[28]

The specific Cu^0 surface area in the reduced catalysts was estimated by adsorptive decomposition of nitrous oxide.[61,62] We assumed the dissociation of nitrous oxide to take place only on the surface of copper according to the reaction $2Cu_{(s)} + N_2O \rightarrow Cu_2O_{(s)} + N_2$. The amount of Cu_2O formed after N_2O chemisorption was determined using TPR. While it was previously established that the optimum temperature range for N_2O adsorption was 60−90 °C,[61−63] our reference Co/SiO_2 sample was also oxidized by N_2O in this temperature range. Therefore, to selectively estimate the Cu surface area, we reduced the adsorption temperature to 35 °C, where we measured an N_2O-related oxidation of the Cu/SiO_2 sample but not of the Co/SiO_2 catalyst. Even in this low temperature range, Cu surface areas were overestimated (Table SI2). Nevertheless, they were

DOI: 10.1021/acs.langmuir.5b04622
Langmuir 2016, 32, 2267−2276

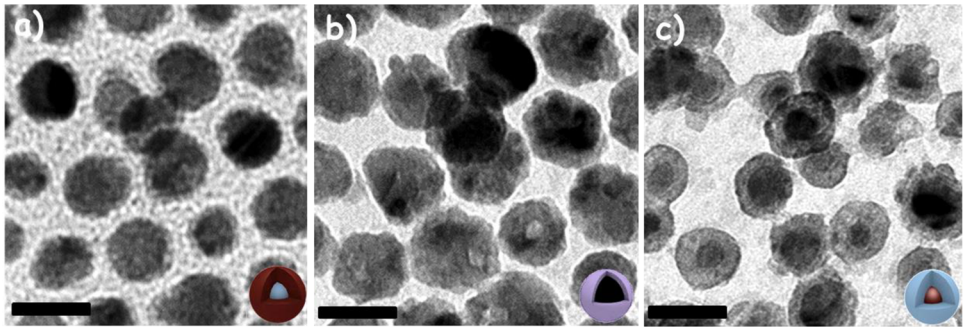

Figure 6. TEM micrographs from the same $Co_{0.3}@Cu_{0.7}$ NPs supported on a SiN_x TEM grid after different treatments: (a) initial $Co_{0.3}@Cu_{0.7}$ NPs; (b) after thermal treatment in air at 350 °C for 4 h; (c) after reduction in 12% H_2−Ar at 350 °C at 30 bar. Scale bar corresponds to 20 nm.

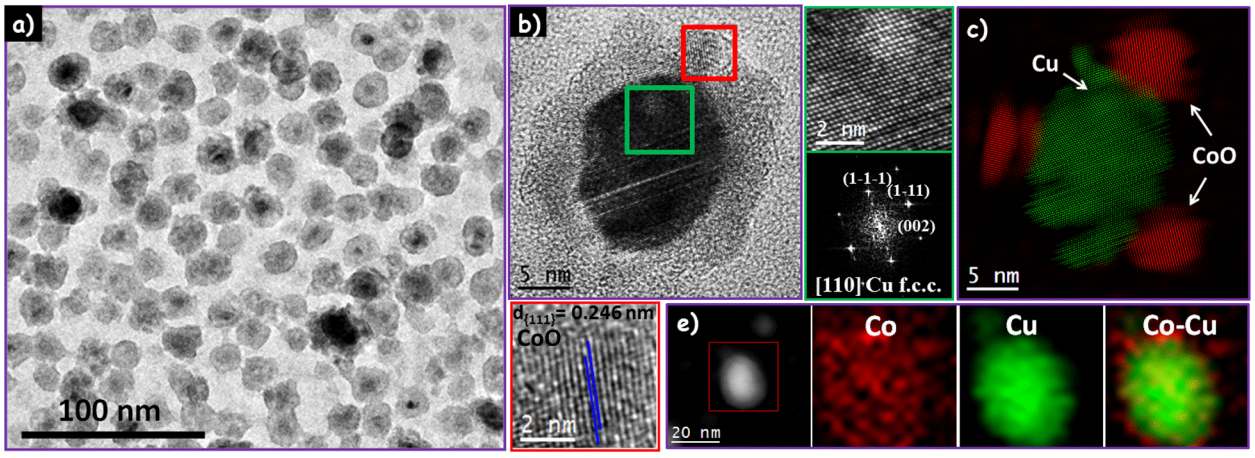

Figure 7. (a) TEM micrographs of $Co_{0.3}@Cu_{0.7}$ NPs oxidized in air at 350 °C for 4 h and reduced in 12% H_2−Ar at 350 °C at 30 bar. (b) HRTEM micrograph of a reduced $Co_{0.3}@Cu_{0.7}$ NPs with details of shell (red squared) and core (green squared) regions and corresponding power spectrum of the core. HRTEM is consistent with a metallic Cu core and a CoO shell. (c) Colorful crystallographic map of the same NP where green indicates the fcc Cu phase and red indicates the fcc CoO phase. (e) EDX compositional maps of a $Co_{0.3}@Cu_{0.7}$ NP after the reduction process.

systematically higher for catalyst with the following compositions Cu/SiO_2 > $Co_{0.3}@Cu_{0.7}/SiO_2$ > $Co_{0.6}@Cu_{0.4}/SiO_2$ > Co/SiO_2 + Cu/SiO_2. These results may indicate that in spite of the core−shell inversion, a significant part of the Cu surface areas were still accessible within $Co_{0.6}@Cu_{0.4}/SiO_2$ and $Co_{0.3}@Cu_{0.7}/SiO_2$ catalysts. This suggests that the Co-based shell was porous and permeable to N_2O or that the surface composition of the Co@Cu NPs after reduction was not pure Co but a Co−Cu alloy which interacted with N_2O. However, N_2O absorption results could be also explained by considering that the presence of a Cu core in direct contact with the Co shell was able to promote Co oxidation by N_2O, although independent Co NPs did not interact with N_2O at 35 °C.

Figure 8 displays the total CO_2 hydrogenation conversion at 30 bar and 3000 h^{-1} over SiO_2-supported monometallic and bimetallic catalysts. Total conversions were much higher for the two reference catalysts containing independent Co NPs than for the pure Cu-based catalyst and the $Co@Cu/SiO_2$ catalysts. Previous works demonstrated that too small Co NPs (<10 nm) showed lower activity in CO_2 hydrogenation[28,35−37] and F-T[12,36,39] reactions and attributed it to a higher susceptibility to oxidation[38] and a related lower capability to dissociate CO.[39] We associate the higher CO_2 conversions of Co/SiO_2-containing catalysts to (i) the higher CO_2 and CO dissociation rates on Co than Cu,[64,65] (ii) the larger size of the Co crystalline domains in the Co/SiO_2 catalysts compared with the $Co@Cu/SiO_2$ catalysts, and (iii) the lower CO_2 hydrogenation activity of the Co shells in $Co@Cu/SiO_2$ catalysts, which could also be related to a higher oxidation susceptibility.

For all catalysts, conversion increased with temperature up to 340 °C. Above this temperature, catalysts containing Co NPs showed a clear decrease in conversion (Figure 8). This is related to a progressive loss of their capacity to produce hydrocarbons when heated at 340 °C and above under reaction conditions (Figures SI8 and SI9). On the other hand, the conversion of the Cu/SiO_2 and $Co@Cu/SiO_2$ catalysts was significantly more stable over time (Figures SI10−SI12).

CO, CH_4, C_2H_6, C_2H_4, C_3H_6, and traces of CH_3OH were the products obtained from the CO_2 hydrogenation reaction over all the catalysts. Nevertheless, each catalyst was characterized by significantly different selectivities to each of these products. The main CO_2 hydrogenation product on Co/SiO_2 was CH_4, with conversion selectivities up to a 70% (Figure 8a). This result is consistent with previous works showing that low space velocities and high pressures favored high selectivities to methane on group 8, 9, and 10 metals supported on SiO_2.[66,67] Furthermore, Co is known to adsorb CO and CO_2 dissociatively in the presence of H_2, leading to the loss of oxygen as water and the production of oxygen-free hydrocarbons. In this catalyst, CO selectivities were in the range between 20% and 40% and increased with temperature in the high temperature range measured as the reverse water gas-shift reaction (RWGS) reaction was favored:[14,15,30]

DOI: 10.1021/acs.langmuir.5b04622
Langmuir 2016, 32, 2267−2276

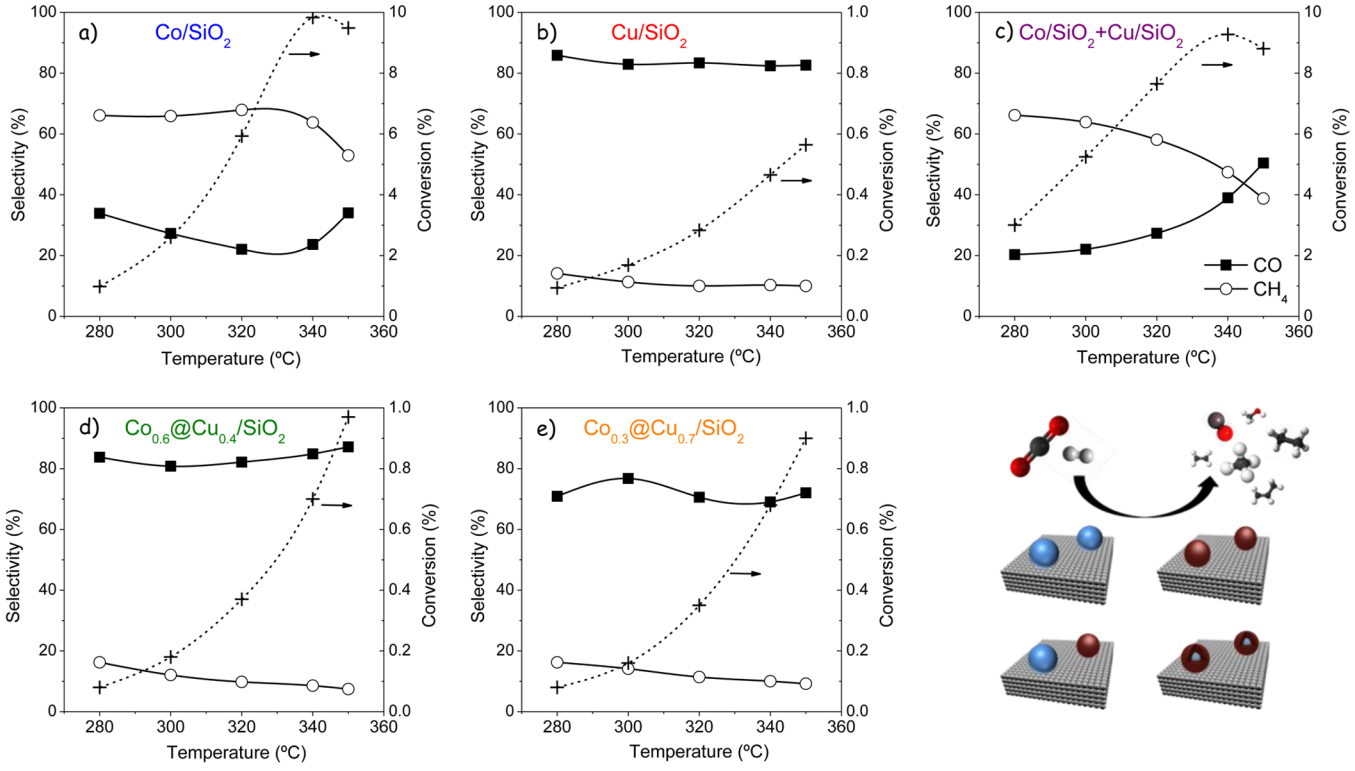

Figure 8. CO_2 conversion and selectivities to CO and CH_4 obtained from Co/SiO_2 (a), Cu/SiO_2 (b), Co/SiO_2 + Cu/SiO_2 (c), $Co_{0.6}@Cu_{0.4}/SiO_2$ (d), and $Co_{0.3}@Cu_{0.7}/SiO_2$ (e) catalysts.

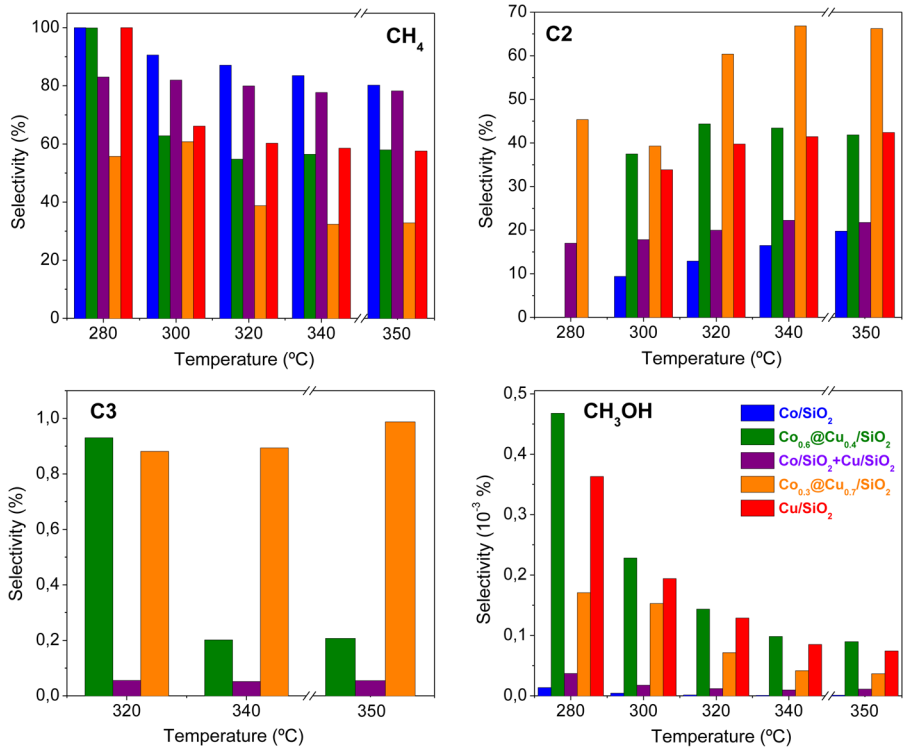

Figure 9. Relative selectivities related to hydrogenated products obtained from the Co/SiO_2, Cu/SiO_2, Co/SiO_2 + Cu/SiO_2, $Co_{0.6}@Cu_{0.4}/SiO_2$, and $Co_{0.3}@Cu_{0.7}/SiO_2$ catalysts.

$$CO_{2(g)} + H_{2(g)} \rightleftarrows CO_{(g)} + H_2O_{(g)} \quad \Delta G_{298\,K} = 28.6\ \text{kJ/mol}$$

The main reaction product of CO_2 hydrogenation on Cu/SiO_2 catalyst was CO, with selectivities up to 85% (Figure 8b). CH_4 was a minor component in the product stream for this catalyst, with selectivities around 10%. This is consistent with the molecular adsorption of CO_2 and CO on Cu and their slow dissociation, which favors alcohol production when combined with the appropriate support.[30−34,68−72]

DOI: 10.1021/acs.langmuir.5b04622
Langmuir 2016, 32, 2267−2276

The catalytic performance of the physical mixture Co/SiO_2 + Cu/SiO_2 was in between that of Co/SiO_2 and Cu/SiO_2, with CH_4 selectivities from 65% to 40% and CO selectivities in the range 20−50% (Figure 8c). On the contrary, $Co@Cu/SiO_2$ catalysts showed much higher tendencies to produce CO, as the Cu/SiO_2 catalyst, and were characterized by relatively low methane selectivities (Figure 8d,e).

Aside from CO and CH_4, C2 and C3 products were also produced with significant rates over monometallic and bimetallic catalysts. The production of higher hydrocarbons requires avoiding the formation of CH_4, as it is the thermodynamically most stable product. To compare the selectivity toward the formation of the different hydrogenated products, Figure 9 displays the relative selectivities (excluding CO) of the different catalysts toward the formation of methane, ethane, ethylene, propene, and methanol.

The relative selectivities to C2 compounds, ethane and ethylene, were much higher for Cu/SiO_2 and $Co@Cu/SiO_2$ than for Co/SiO_2 and Co/SiO_2 + Cu/SiO_2 catalysts. 40−65% relative selectivities toward de formation of C2 products were obtained for $Co@Cu/SiO_2$ catalysts above 300 °C. Furthermore, propene was only detected on the bimetallic catalysts, with much higher selectivities for the $Co@Cu/SiO_2$ than for Co/SiO_2 + Cu/SiO_2 catalysts. The higher relative selectivities of $Co@Cu/SiO_2$ catalysts to carbon chain growth confirmed the positive synergy between the two metals when combined within the same particle.

Methanol selectivities were very low for all catalysts (Figure 9). We associate this experimental fact to the need for a more suitable support than silica.[72] It is generally accepted that Cu is the active phase for methanol formation.[30−34,68−72] However, the support plays an extremely important role, and oxide supports such as ZnO, ZrO_2, or Al_2O_3 have been found essential to promote the methanol formation. As expected, Cu-containing catalyst showed much higher relative methanol selectivities than Co/SiO_2. Furthermore, $Co@Cu/SiO_2$ catalysts also showed relative selectivities to methanol well beyond those of Co/SiO_2 + Cu/SiO_2 catalyst (Figure 9).

Catalysts were further analyzed after reaction. Figure 10a shows the XRD patterns of the initial $Co_{0.3}@Cu_{0.7}$ NPs and of the $Co_{0.3}@Cu_{0.7}/SiO_2$ catalyst after the reduction treatment and after catalytic test. Notice that the cubic structure of the NPs was conserved. The narrower peaks after reduction and after reaction are related to a better crystallinity of the material after thermal treatment of the sample at 350 °C and under 30 bar of pressure. On the other hand, single particle compositional analysis of the $Co_{0.3}@Cu_{0.7}$ NPs supported on a silicon nitride TEM grid and exposed to the oxidation, reduction, and reaction conditions showed the core−shell structure not to stand the reaction conditions. During reaction conditions, the two metal phases separated to form nonsymmetric bimetallic heterostructures (Figure 10b).

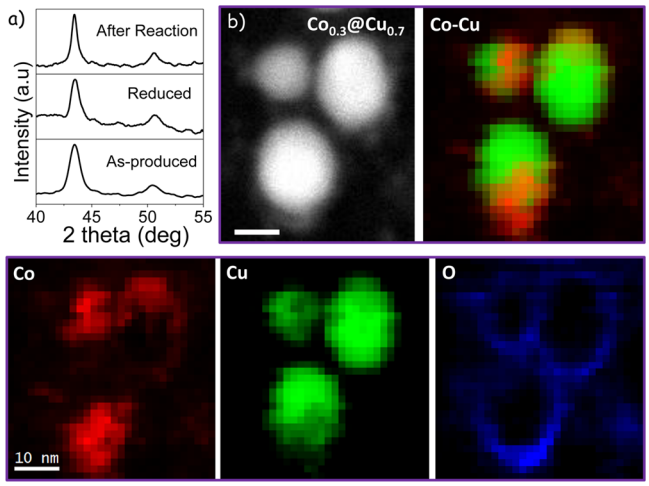

Figure 10. (a) XRD patterns of the initial $Co_{0.3}@Cu_{0.7}$ NPs and of the $Co_{0.3}@Cu_{0.7}/SiO_2$ catalyst after the reduction treatment and after the catalytic test. (b) HAADF-STEM micrograph and EELS chemical composition maps, Co (red), Cu (green), and O (blue), of three $Co_{0.3}@Cu_{0.7}$ NPs supported on a silicon nitride TEM grid and exposed to the consecutive, oxidation, reduction, and reaction conditions. Scale bar = 10 nm.

4. CONCLUSIONS

A new colloidal synthesis route to produce Co−Cu NPs with controlled composition based on the galvanic replacement of Co by Cu was detailed. This synthetic strategy allowed the preparation of Co−Cu model catalysts with well-controlled parameters to be studied in real working conditions. These catalysts were thoroughly characterized to understand the interactions originated at the nanoscale between the two metals. TPR profiles showed a synergistic effect on the reduction of cobalt and copper in $Co−Cu/SiO_2$ catalysts. During oxidation and posterior reduction, a core−shell inversion was observed without coalescence or aggregation of the nanoparticles. We believe Co intermixed with Cu during the oxidation process and Cu reduced to the center of the NP during the reduction treatment, while Co migrated at its surface. Nevertheless, N_2O chemisorption pointed out the accessibility of the copper within the reversed Co−Cu core−shell NPs. CO_2 conversion tests showed that catalysts containing large and pure Co NPs were characterized by 1 order of magnitude higher total conversions. Nevertheless, a clear synergism between Co and Cu was shown by the different TPR profiles and catalytic behavior in CO_2 hydrogenation; $Co−Cu/SiO_2$ showed a better stability and higher relative selectivities to form C−C bonds and methanol than monometallic catalysts and the physical mixture Co/SiO_2 + Cu/SiO_2. A more appropriate support than SiO_2 and possibly larger Co domains would be necessary to improve both the total CO_2 conversion and the selectivity toward high hydrocarbons and especially alcohols.

■ ASSOCIATED CONTENT

Ⓢ Supporting Information

The Supporting Information is available free of charge on the ACS Publications website at DOI: 10.1021/acs.langmuir.5b04622.

ICP metal contents, Cu surface areas, thermogravimetry results, additional TEM and HRTEM micrographs, X-ray photoelectron spectroscopy (XPS) analysis of the material after rection and time evolution of total CO_2 conversions (PDF)

■ AUTHOR INFORMATION

Corresponding Authors

*E-mail: narcis.homs@qi.ub.es (N.H.).
*E-mail: acabot@irec.cat (A.C.).

Notes

The authors declare no competing financial interest.

DOI: 10.1021/acs.langmuir.5b04622
Langmuir 2016, 32, 2267−2276

■ ACKNOWLEDGMENTS

The research was supported by the European Regional Development Funds and the Spanish MICINN projects CSD2009-00050, MAT2014-52416-P, and ENE2013-46624-C4-3-R. M.I. thanks AGAUR for her Beatriu de Pinós postdoctoral grant 2013 BP-A00344. J.A. and A.G. acknowledge the funding from the Spanish MINECO Severo Ochoa Excellence Program and Generalitat de Catalunya 2014SGR1638.

■ REFERENCES

(1) Somorjai, G. A.; Park, J. Y. Molecular Factors of Catalytic Selectivity. *Angew. Chem., Int. Ed.* **2008**, *47*, 9212−9228.
(2) Jia, C. J.; Schüth, F. Colloidal Metal Nanoparticles as a Component of Designed Catalyst. *Phys. Chem. Chem. Phys.* **2011**, *13*, 2457−2487.
(3) Zaera, F. Nanostructured Materials for Applications in Heterogeneous Catalysis. *Chem. Soc. Rev.* **2013**, *42*, 2746−2762.
(4) Gross, E.; Somorjai, G. A. Molecular Catalysis Science: Nanoparticle Synthesis and Instrument Development for Studies Under Reaction Conditions. *J. Catal.* **2015**, *328*, 91−101.
(5) Yin, Y.; Alivisatos, A. P. Colloidal Nanocrystal Synthesis and the Organic−Inorganic Interface. *Nature* **2005**, *437*, 664−670.
(6) Luo, Z.; Ibáñez, M.; Antolín, A. M.; Genç, A.; Shavel, A.; Contreras, S.; Medina, F.; Arbiol, J.; Cabot, A. Size and Aspect Ratio Control of Pd_2Sn Nanorods and Their Water Denitration Properties. *Langmuir* **2015**, *31*, 3952−3957.
(7) Yu, X.; Shavel, A.; An, X.; Luo, Z.; Ibáñez, M.; Cabot, A. The Effect of the Ga Content on the Photocatalytic Hydrogen Evolution of $CuIn_{1-x}Ga_xS_2$ Nanocrystals. *J. Am. Chem. Soc.* **2014**, *136*, 9236−9239.
(8) Ibáñez, M.; Cabot, A. All Change for Nanocrystals. *Science* **2013**, *340*, 935−936.
(9) Kovalenko, M. V.; et al. Prospects of Nanoscience with Nanocrystals. *ACS Nano* **2015**, *9*, 1012−1057.
(10) Nafria, R.; de la Piscina, P. R.; Homs, N.; Morante, J. R.; Cabot, A.; Diaz, U.; Corma, A. Embedding Catalytic Nanoparticles Inside Mesoporous Structures with Controlled Porosity: $Au@TiO_2$. *J. Mater. Chem. A* **2013**, *1*, 14170−14176.
(11) Flox, C.; Rubio-Garcia, J.; Nafria, R.; Zamani, R.; Skoumal, M.; Andreu, T.; Arbiol, J.; Cabot, A.; Morante, J. R. Active Nano-$CuPt_3$ Electrocatalyst Supported on Graphene for Enhancing Reactions at the Cathode in all-Vanadium Redox Flow Batteries. *Carbon* **2012**, *50*, 2372−2374.
(12) Herranz, T.; Deng, X.; Cabot, A.; Guo, J.; Salmeron, M. Influence of the Cobalt Particle Size in the CO Hydrogenation Reaction Studied by in Situ X-Ray Absorption Spectroscopy. *J. Phys. Chem. B* **2009**, *113*, 10721−10727.
(13) Kwangjin, A.; Somorjai, G. A.; Nanocatalysis, I. Synthesis of Metal and Bimetallic Nanoparticles and Porous Oxides and Their Catalytic Reaction Studies. *Catal. Lett.* **2015**, *145*, 233−248.
(14) Wang, W.; Wang, S.; Ma, X.; Gong, J. Recent Advances in Catalytic Hydrogenation of Carbon Dioxide. *Chem. Soc. Rev.* **2011**, *40*, 3703−3727.
(15) Homs, N.; Toyir, J.; de la Piscina, P. R. Catalytic Processes for Activation of CO_2. *New and future Developments in Catalysis*; Elsevier: 2013.
(16) Centi, G.; Perathoner, S. Opportunities and Prospects in the Chemical Recycling of Carbon Dioxide to Fuels. *Catal. Today* **2009**, *148*, 191−205.
(17) Ma, J.; Sun, N.; Zhang, X.; Zhao, N.; Xiao, F.; Wei, W.; Sun, Y. A Short Review of Catalysis for CO_2 Conversion. *Catal. Today* **2009**, *148*, 221−231.
(18) Nieskens, D. L.; Ferrari, D.; Liu, Y.; Kolonko, R. The Conversion of Carbon Dioxide and Hydrogen into Methanol and Higher Alcohols. *Catal. Commun.* **2011**, *14*, 111−113.
(19) Courty, P.; Durand, D.; Freund, E.; Sugier, A. C_1-C_6 Alcohols From Synthesis Gas on Copper-Cobalt Catalysts. *J. Mol. Catal.* **1982**, *17*, 241−254.
(20) Dalmon, J. A.; Chaumette, P.; Mirodatos, C. Higher Alcohols Synthesis on Cobalt Based Model Catalysts. *Catal. Today* **1992**, *15*, 101−127.
(21) Mouaddib, N.; Perrichon, V.; Martin, G. A. Characterization of Copper-Cobalt Catalysts for Alcohol Synthesis from Syngas. *Appl. Catal., A* **1994**, *118*, 63−72.
(22) Bailliard-Letournel, R. M.; Cobo, A. J. G.; Mirodatos, C.; Primet, M.; Dalmon, J. A. About the Nature of the Co-Cu Interaction in Co-Based Catalysts for Higher Alcohols Synthesis. *Catal. Lett.* **1989**, *2*, 149−156.
(23) Cao, R.; Pan, W. X.; Griffin, G. L. Direct Synthesis of Higher Alcohols Using Bimetallic Copper/Cobalt Catalysts. *Langmuir* **1988**, *4*, 1108−1112.
(24) Liu, G.; Niu, T.; Pan, D.; Liu, F.; Liu, Y. Preparation of Bimetal Cu−Co Nanoparticles Supported on Meso−Macroporous SiO_2 and Their Application to Higher Alcohols Synthesis from Syngas. *Appl. Catal., A* **2014**, *483*, 10−18.
(25) Xiang, Y.; Barbosa, R.; Kruse, N. Higher Alcohols Through CO Hydrogenation over CoCu Catalysts: Influence of Precursor Activation. *ACS Catal.* **2014**, *4*, 2792−2800.
(26) Nilekar, A. U.; Alayoglu, S.; Eichhorn, B.; Mavrikakis, M. Preferential CO Oxidation in Hydrogen: Reactivity of Core−Shell Nanoparticles. *J. Am. Chem. Soc.* **2010**, *132*, 7418−7428.
(27) Subramanian, N. D.; Balaji, G.; Kumar, C. S. S. R.; Spivey, J. Development of Cobalt−Copper Nanoparticles as Catalysts for Higher Alcohol Synthesis from Syngas. J. *Catal. Today* **2009**, *147*, 100−106.
(28) Alayoglu, S.; Beaumont, S. K.; Melaet, G.; Lindeman, A. E.; Musselwhite, N.; Brooks, C. J.; Somorjai, G. A. Surface Composition Changes of Redox Stabilized Bimetallic CoCu Nanoparticles Supported on Silica under H_2 and O_2 Atmospheres and During Reaction between CO_2 and H_2: In Situ X-ray Spectroscopic Characterization. *J. Phys. Chem. C* **2013**, *117*, 21803−21809.
(29) Khodakov, A. Y.; Chu, W.; Fongarland, P. Advances in the Development of Novel Cobalt Fischer−Tropsch Catalysts for Synthesis of Long-Chain Hydrocarbons and Clean Fuels. *Chem. Rev.* **2007**, *107*, 1692−1744.
(30) Spivey, J. J.; Egbebi, A. Heterogeneous Catalytic Synthesis of Ethanol from Biomass-Derived Syngas. *Chem. Soc. Rev.* **2007**, *36*, 1514−1528.
(31) Gupta, M.; Smith, M. L.; Spivey, J. J. Heterogeneous Catalytic Conversion of Dry Syngas to Ethanol and Higher Alcohols on Cu-based Catalysts. *ACS Catal.* **2011**, *1*, 641−656.
(32) Waugh, K. C. Methanol Synthesis. *Catal. Today* **1992**, *15*, 51−75.
(33) Klier, K. Methanol Synthesis. *Adv. Catal.* **1982**, *31*, 243−313.
(34) Toyir, J.; de la Piscina, P. R.; Fierro, J. L. G.; Homs, N. Highly Effective Conversion of CO_2 to Methanol over Supported and Promoted Copper-based Catalysts: Influence of Support and Promoter. *Appl. Catal., B* **2001**, *29*, 207−215.
(35) Iablokov, V.; Beaumont, S. K.; Alayoglu, S.; Pushkarev, V. V.; Specht, C.; Gao, J.; Somorjai, G. A. Size-Controlled Model Co Nanoparticle Catalysts for CO_2 Hydrogenation: Synthesis, Characterization, and Catalytic Reactions. *Nano Lett.* **2012**, *12*, 3091−3096.
(36) Melaet, G.; Ralston, W. T.; Li, C. S.; Alayoglu, S.; An, K.; Musselwhite, N.; Somorjai, G. A. Evidence of Highly Active Cobalt Oxide Catalyst for the Fischer−Tropsch Synthesis and CO_2 Hydrogenation. *J. Am. Chem. Soc.* **2014**, *136*, 2260−2263.
(37) Melaet, G.; Lindeman, A. E.; Somorjai, G. A. Cobalt Particle Size Effects in the Fischer−Tropsch Synthesis and in the Hydrogenation of CO_2 Studied with Nanoparticle Model Catalysts on Silica. *Top. Catal.* **2014**, *57*, 500−507.
(38) Wang, Z. J.; Skiles, S.; Yang, F.; Yan, Z.; Goodman, D. W. Particle Size Effects in Fischer−Tropsch Synthesis by Cobalt. *Catal. Today* **2012**, *181*, 75−81.
(39) Tuxen, A.; Carenco, S.; Chintapalli, M.; Chuang, C. H.; Escudero, C.; Pach, E.; Salmeron, M. Size-Dependent Dissociation of Carbon Monoxide on Cobalt Nanoparticles. *J. Am. Chem. Soc.* **2013**, *135*, 2273−2278.
(40) Natesakhawat, S.; Lekse, J. W.; Baltrus, J. P.; Ohodnicki, P. R., Jr.; Howard, B. H.; Deng, X.; Matranga, C. Active Sites and Structure−

DOI: 10.1021/acs.langmuir.5b04622
Langmuir 2016, 32, 2267−2276

Activity Relationships of Copper-Based Catalysts for Carbon Dioxide Hydrogenation to Methanol. *ACS Catal.* **2012**, *2*, 1667−1676.
(41) Prieto, G.; Beijer, S.; Smith, M. L.; He, M.; Au, Y.; Wang, Z.; Bruce, D. A.; de Jong, K. P.; Spivey, J. J.; de Jongh, P. E. Design and Synthesis of Copper−Cobalt Catalysts for the Selective Conversion of Synthesis Gas to Ethanol and Higher Alcohols. *Angew. Chem., Int. Ed.* **2014**, *53*, 6397−6401.
(42) Carenco, S.; Tuxen, A.; Chintapali, M.; Pach, E.; Escudero, C.; Ewers, T. D.; Jiang, P.; Borondics, F.; Thornton, G.; Alivastos, A. P.; Bluhm, H.; Guo, J.; Salmeron, M. Dealloying of Cobalt from CuCo Nanoparticles Under Syngas Exposure. *J. Phys. Chem. C* **2013**, *117*, 6259−6266.
(43) Puntes, V. F.; Krishnan, K. M.; Alivisatos, A. P. Colloidal Nanocrystal Shape and Size Control: the Case of Cobalt. *Science* **2001**, *291*, 2115−2117.
(44) Hung, L. I.; Tsung, C. K.; Huang, W.; Yang, P. Room-Temperature Formation of Hollow Cu_2O Nanoparticles. *Adv. Mater.* **2010**, *22*, 1910−1914.
(45) Rioux, R. M.; Song, H.; Hoefelmeyer, J. D.; Yang, P.; Somorjai, G. A. High-Surface-Area Catalyst Design: Synthesis, Characterization, and Reaction Studies of Platinum Nanoparticles in Mesoporous SBA-15 Silica. *J. Phys. Chem. B* **2005**, *109*, 2192−2202.
(46) Xia, X.; Wang, Y.; Ruditskiy, A.; Xia, Y. 25th Anniversary Article: Galvanic Replacement: A Simple and Versatile Route to Hollow Nanostructures with Tunable and Well-Controlled Properties. *Adv. Mater.* **2013**, *25*, 6313−6333.
(47) Dinega, D. P.; Bawendi, M. G. A Solution-Phase Chemical Approach to a new Crystal Structure of Cobalt. *Angew. Chem., Int. Ed.* **1999**, *38*, 1788−1791.
(48) *ASM Handbook; Alloy Phase Diagrams*; ASM International: 1992; Vol. 3.
(49) Ahmed, J.; Ganguly, A.; Saha, S.; Gupta, G.; Trinh, P.; Mugweru, A. M.; Ganguli, A. K. Enhanced Electrocatalytic Activity of Copper−Cobalt Nanostructures. *J. Phys. Chem. C* **2011**, *115*, 14526−14533.
(50) Li, G.; Wang, Q.; Li, D.; Lü, X.; He, J. Structure Evolution During the Cooling and Coalesced Cooling Processes of Cu−Co Bimetallic Clusters. *Phys. Lett. A* **2008**, *372*, 6764−6769.
(51) de la Peña O'Shea, V. A.; Homs, N.; Pereira, E. B.; Nafria, R.; Ramírez de la Piscina, P. X-ray Diffraction Study of Co_3O_4 Activation Under Ethanol Steam-Reforming. *Catal. Today* **2007**, *126*, 148−152.
(52) Khodakov, A. Y.; Lynch, J.; Bazin, D.; Rebours, B.; Zanier, N.; Moisson, B.; Chaumette, P. Reducibility of Cobalt Species in Silica-Supported Fischer−Tropsch Catalysts. *J. Catal.* **1997**, *168*, 16−25.
(53) Smith, M. L.; Campos, A.; Spivey, J. J. Reduction Processes in Cu/SiO_2, Co/SiO_2, and CuCo/SiO_2 Catalysts. *Catal. Today* **2012**, *182*, 60−66.
(54) Fierro, G.; Jacono, M. L.; Inversi, M.; Dragone, R.; Porta, P. TPR and XPS Study of Cobalt−Copper Mixed Oxide Catalysts: Evidence of a Strong Co−Cu Interaction. *Top. Catal.* **2000**, *10*, 39−48.
(55) Deng, S.; Chu, W.; Xu, H.; Shi, L.; Huang, L. Effects of Impregnation Sequence on the Microstructure and Performances of Cu-Co Based Catalysts for the Synthesis of Higher Alcohols. *J. Nat. Gas Chem.* **2008**, *17*, 369−373.
(56) Cesar, D. V.; Peréz, C. A.; Salim, V. M. M.; Schmal, M. Stability and Selectivity of Bimetallic Cu−Co/SiO_2 Catalysts for Cyclohexanol Dehydrogenation. *Appl. Catal., A* **1999**, *176*, 205−212.
(57) Yin, Y.; Erdonmez, C. K.; Cabot, A.; Hughes, S.; Alivisatos, A. P. Colloidal Synthesis of Hollow Cobalt Sulfide Nanocrystals. *Adv. Funct. Mater.* **2006**, *16*, 1389−1399.
(58) Ibáñez, M.; Fan, J.; Li, W.; Cadavid, D.; Nafria, R.; Carrete, A.; Cabot, A. Means and Limits of Control of the Shell Parameters in Hollow Nanoparticles Obtained by the Kirkendall Effect. *Chem. Mater.* **2011**, *23*, 3095−3104.
(59) Cabot, A.; Ibáñez, M.; Guardia, P.; Alivisatos, A. P. Reaction regimes on the synthesis of holoow particles by the Kirkendall effect. *J. Am. Chem. Soc.* **2009**, *131*, 11326−11328.
(60) Cabot, A.; Puntes, F. F.; Shevchenko, E.; Yin, Y.; Balcells, L.; Marcus, M. A.; Hughes, S. M.; Alivisatos, A. P. Vacancy coalescence during oxidation of iron nanoparticles. *J. Am. Chem. Soc.* **2007**, *129*, 10358−10360.
(61) Evans, J. W.; Wainwright, M. S.; Bridgewater, A. J.; Young, D. J. On the Determination of Copper Surface Area by Reaction with Nitrous Oxide. *Appl. Catal.* **1983**, *7*, 75−83.
(62) Robinson, W. R. A. M.; Mol, J. C. Characterization and Catalytic Activity of Copper/Alumina Methanol Synthesis Catalysts. *Appl. Catal.* **1988**, *44*, 165−177.
(63) Mahdavi, V.; Peyrovi, M. H. Synthesis of C_1−C_6 Alcohols Over Copper/Cobalt Catalysts: Investigation of the Influence of Preparative Procedures on the Activity and Selectivity of Cu−Co_2O_3/ZnO, Al_2O_3 Catalyst. *Catal. Commun.* **2006**, *7*, 542−549.
(64) Lahtinen, J.; Anraku, T.; Somorjai, G. A. C, CO and CO_2 Hydrogenation on Cobalt Foil Model Catalysts: Evidence for the Need of CoO Reduction. *Catal. Lett.* **1994**, *25*, 241−255.
(65) Sandoval, M. J.; Bell, A. T. Temperature-Programmed Desorption Studies of the Interactions of H_2, CO, and CO_2 with Cu/SiO_2. *J. Catal.* **1993**, *144*, 227−237.
(66) Barbier, A.; Tuel, A.; Arcon, I.; Kodre, A.; Martin, G. A. Characterization and Catalytic Behavior of Co/SiO_2 Catalysts: Influence of Dispersion in the Fischer−Tropsch Reaction. *J. Catal.* **2001**, *200*, 106−116.
(67) Weatherbee, G. D.; Bartholomew, C. H. Hydrogenation of CO_2 on Group VIII Metals: IV. Specific Activities and Selectivities of Silica-Supported Co, Fe, and Ru. *J. Catal.* **1984**, *87*, 352−362.
(68) Fujitani, T.; Nakamura, I.; Uchijima, T.; Nakamura, J. The Kinetics and Mechanism of Methanol Synthesis by Hydrogenation of CO_2 over a Zn-deposited Cu (111) Surface. *Surf. Sci.* **1997**, *383*, 285−298.
(69) Clancy, P.; Breen, J. P.; Ross, J. R. The Preparation and Properties of Coprecipitated Cu−Zr−Y and Cu−Zr−La Catalysts used for the Steam Reforming of Methanol. *Catal. Today* **2007**, *127*, 291−294.
(70) Chinchen, G. C.; Waugh, K. C.; Whan, D. A. The Activity and State of the Copper Surface in Methanol Synthesis Catalysts. *Appl. Catal.* **1986**, *25*, 101−107.
(71) Fujitani, T.; Nakamura, J. The Effect of ZnO in Methanol Synthesis Catalysts on Cu Dispersion and the Specific Activity. *Catal. Lett.* **1998**, *56*, 119−124.
(72) Robbins, J. L.; Iglesia, E.; Kelkar, C. P.; DeRites, B. Methanol Synthesis over Cu/SiO_2 Catalysts. *Catal. Lett.* **1991**, *10*, 1−10.

DOI: 10.1021/acs.langmuir.5b04622
Langmuir 2016, 32, 2267−2276